FLOW DISTRIBUTION AROUND THE SSME MAIN INJECTOR ASSEMBLY USING POROSITY FORMULATION

Gary C. Cheng[*]
SECA, Inc, Huntsville, AL 35805

/N   *- - /L*

Yen-Sen Chen[†]
ESI, Huntsville, AL 35805

and
Ten-See Wang[‡]
NASA Marshall Space Flight Center, Huntsville, AL 35812

ABSTRACT

Hot gas turbulent flow distribution around the main injector assembly of the Space Shuttle Main Engine (SSME) and Liquid Oxidizer (LOX) flow distribution through the LOX posts have a great effect on the combustion phenomena inside the main combustion chamber. In order to design a CFD model to be an effective engineering analysis tool with good computational turn-around time (especially for 3-D flow problems) and still maintain good accuracy in describing the flow features, the concept of porosity was employed to describe the effects of blockage and drag force due to the presence of the LOX posts in the turbulent flow field around the main injector assembly of the SSME. 2-D numerical studies were conducted to identify the drag coefficients of the flows both through tube banks and around the shielded posts over a wide range of Reynolds numbers. Empirical, analytical expressions of the drag coefficient as a function of local flow Reynolds number were then deduced. The porosity model was applied to the turbulent flow around the main injector assembly of the SSME, and analyses were performed. The 3-D CFD analysis was divided into three parts, LOX dome, hot gas injector assembly, and hydrogen cavity. The numerical results indicate that the mixture ratio at the downstream of injector face was close to stoichiometric around baffle elements.

NOMENCLATURE

A	global flow exit area
A_i	local flow exit area
C_1, C_2, C_3	turbulence modeling constants
C_D	drag coefficient
C_μ	turbulence modeling constant

[*] Research Engineer, Member AIAA.

[†] President, Member AIAA.

[‡] Team Leader, Computational Fluid Dynamics Branch, Member AIAA.

D	drag force
F_c	convective flux
F_i	numerical fluxes in the transformed coordinates
F_v	viscous flux
G_{ij}	diffusion metrics
H_f	heat flux
J	Jacobian of coordinate transformation
K	local loss coefficient
K'	global loss coefficient
k	turbulence kinetic energy
$\dot{M}$	global exit mass flow rate through a type of porous medium
$\dot{m}$	local exit mass flow rate through a type of porous medium
N	number of posts for a type of element
P_r	turbulence kinetic energy production rate
p	static pressure
p_{baffle}	static pressure in the combustion chamber near the end of baffle elements
$p_{chamber}$	static pressure in the combustion chamber near the injector plate
Q_t	heat source
q	flow primitive variables
Re	Reynolds number
R_q	numerical residual of the governing equations
S_q	source terms of the governing equations
t	time
U_i	transformed (contravariant) velocities
u^+	nondimensional velocity
u_i	velocity vectors
u_τ	friction velocity ($\equiv \sqrt{\tau_w/\rho}$)
x, y, z	Cartesian coordinates
y^+	nondimensional normal distance away from the wall
ε	turbulence kinetic energy dissipation rate
Φ	energy dissipation
γ_i	surface porosity
γ_v	volume porosity
μ_e	effective viscosity
μ_l	fluid viscosity
μ_t	eddy viscosity
ω_n	species production rate
ρ	fluid density
σ_q	turbulence modeling constant
ξ, η, ς	transformed curvilinear coordinates
ξ_i	transformed curvilinear coordinate directions

INTRODUCTION

Fluid flow and heat transfer in the main injector assembly of the SSME are complex phenomena. The basic understanding of these phenomena is essential to achieving optimum performance during normal operating conditions and maintaining structural integrity during off-design operations. The mixture ratio and mass flow rate distributions of the SSME main injector assembly will greatly affect 1) engine performance, and 2) heat loads of the combustion chamber; especially, the later effect is directly linked to the durability of the engine. Historically, the SSME has been suffering burn out of the LOX post baffle elements and erosion of the combustion chamber during firings. In order to investigate possible causes of such damage, understanding the flow field at main injector exit is essential. The geometry of the SSME main injector assembly is extremely complex as shown in Figure 1, and its flow field is three-dimensional and turbulent. Conventional three-dimensional computational fluid dynamic (CFD) models are not practical to describe the necessary geometric detail of the SSME main injector assembly. The flow description was simplified by utilizing the concept of porosity to provide an effective engineering design tool for this system.

The objective of this study was to develop a practical CFD simulation of the main injector assembly. The geometric complexity caused by the use of hundreds of individual LOX-post elements was reduced to a manageable computation by using non-isotropic porosity and distributed resistance models. LOX-post arrays, shielded LOX-posts, and flows through porous injector plates were characterized with blockage and resistance models. A non-isotropic porosity model was incorporated into an existing Navier-Stokes flow solver (FDNS). Volume and surface porosity parameters, which are based on the configurations of local lox-post clustering, were introduced into the governing equations. Accuracy and robustness of the proposed model was demonstrated through data comparisons with benchmark test data and with detailed CFD solutions. Application of the postulated model to the turbulent flow within the main injector assembly of the SSME was made. This design tool predicts the local O/F distribution of the flow entering the main combustion chamber.

CFD METHODOLOGY

The turbulent flow around the LOX post assembly is similar to the flow through a tube bank ensemble. There are basically three methods available in the literature[1] to analyze the fluid dynamics and heat transfer characteristics of flow-cylinder assemblies with various configurations. These methods are: 1) sub-channel analysis; 2) porosity and distributed resistance approach[2]; and 3) rod-bundle fluid/thermal dynamics analysis using boundary fitted coordinate (BFC) system[3-4]. The first method is a simplified approach of the second method. Although the last method of analysis can provide the most detailed computational results, the mesh size required to resolve the geometrical complexity of an entire main injector assembly prohibits its use as an effective engineering design/analysis tool. One solution for this problem is the use of porosity modeling in the CFD analysis which will provide much better computer turn-around time. Validity of the approximations employed in the porosity model can be verified by comparing with the detailed

3

CFD/BFC solutions for geometrically simplified test cases. A non-isotropic porosity model was developed and validated by comparing to the 2-D tube bank flows over a wide range of Reynolds numbers. The mass flow rate through the post element and the porous plate was also calculated by using the distributed resistance model. The non-isotropic porosity and the distributed resistance models were incorporated into the Navier-Stokes flow solver (FDNS).

GOVERNING EQUATIONS

The FDNS code[5-7] is a time-accurate pressure-based predictor-corrector flow solver. Various turbulence models, such as standard k-ε mode, extended k-ε model[8], low Reynolds number k-ε model, along with different compressibility corrections[6-7], have also been incorporated into the code. The FDNS code was employed to solve a set of non-linear and coupled transport equations, including the continuity equation, Navier-Stokes equations, energy equation, and two-equation turbulence models, in curvilinear coordinates. The system of governing equations can be generalized and expressed as

$$\frac{1}{J}\frac{\partial \rho q}{\partial t} = -\frac{\partial F_i}{\partial \xi_i} + S_q = R_q = \text{Residual} \tag{1}$$

where ρ and q (= 1, u, v, w, h, k, ε, and α_n) denote the fluid density and the flow primitive variables for the continuity, momentum, energy, turbulence kinetic energy, turbulence dissipation rate, and species mass fractions, respectively. The numerical flux, F, is the sum of a convective flux, F_c, and a viscous flux, F_v, i.e.

$$F = F_c + F_v , \qquad F_c = \rho U_i q , \qquad F_v = -\mu_e G_{ij}\frac{\partial q}{\partial \xi_i} \tag{2}$$

where J, U_i and G_{ij} represent the Jacobian of the coordinate transformation, transformed velocities, and diffusion metrics, respectively. They are written as

$$J = \frac{\partial(\xi,\eta,\zeta)}{\partial(x,y,z)} , \qquad U_i = \frac{u_i}{J}\frac{\partial \xi_i}{\partial x_j} , \qquad G_{ij} = \frac{1}{J}\frac{\partial \xi_i}{\partial x_k}\frac{\partial \xi_j}{\partial x_k} \tag{3}$$

$\mu_e = (\mu_l + \mu_t)/\sigma_q$ is the effective viscosity when the turbulent eddy viscosity concept is employed to model the turbulent flows, while μ_l is the fluid viscosity. The turbulence eddy viscosity μ_t can be correlated as, $\mu_t = \rho C_\mu k^2/\varepsilon$, and C_μ and σ_q denote turbulence modeling constants. Source terms S_q in the governing equations can be written as

4

$$S_q = \frac{1}{J} \left\{ \begin{array}{c} 0 \\[6pt] -p_x + \nabla[\mu_e(u_j)_x] - \frac{2}{3}(\mu_e \nabla u_j)_x + F_x J \\[6pt] -p_y + \nabla[\mu_e(u_j)_y] - \frac{2}{3}(\mu_e \nabla u_j)_y + F_y J \\[6pt] -p_z + \nabla[\mu_e(u_j)_z] - \frac{2}{3}(\mu_e \nabla u_j)_z + F_z J \\[6pt] Dp/Dt + \Phi + Q_t \\[6pt] \rho(P_r - \varepsilon) \\[6pt] \frac{\rho}{k}(C_1 P_r \varepsilon - C_2 \varepsilon^2 + C_3 P_r^2) \\[6pt] \omega_n, \qquad n = 1,\ldots\ldots N \end{array} \right\} \tag{4}$$

where p and u_j are the static pressure and velocity vectors, P_r is the turbulence kinetic energy production rate, ω_n is the species production rate, where C_1, C_2, and C_3 (= 1.15, 1.92, and 0.25) are turbulence modeling constants of the extended k-ε turbulence model. The extended k-ε turbulence model, used as the baseline model in the present study, has shown the capability of providing good predictions for complex turbulent flows such as mixing shear layers and effects of curvature and separation[8-9]. F_x, F_y, and F_z are the forces in x-, y-, and z-axis directions, respectively, due to the presence of LOX posts. Φ and Q_t stand for the energy dissipation and heat source in the energy equation. The equation of state for an ideal gas or for a real gas is used to close the above system of equations.

A modified wall function approach is employed to provide good near-wall approximation which is less sensitive to near-wall grid spacing. Unlike the conventional wall function treatment, in which the non-dimensionalized quantities ($y^+ \equiv \rho u_\tau y/\mu$ and $u^+ \equiv u/u_\tau$) are not well-defined in regions with flow separation, the present approach adopts the complete velocity profile suggested by Liakopoulos[10]. The formulation for the wall function can be expressed as

$$u^+ = ln\left[\frac{(y^+ + 11)^{4.02}}{(y^{+2} - 7.37y^+ + 83.3)^{0.79}} \right] + 5.63\, tan^{-1}(0.12y^+ - 0.441) - 3.81 \tag{5}$$

This velocity profile provides a smooth transition between logarithmic law of the wall and linear viscous sublayer variation. Based on the profile, the turbulent shear stress and near-wall turbulence energy production rate can be calculated properly.

NUMERICAL ALGORITHM

In the proposed flow solver, FDNS code, finite difference approximations are employed to discretized the transport equations on non-stagger grid systems. A second-order time-centered or an implicit Euler time-marching scheme is utilized to solve the transient or steady state flow problem. For the space discretization, high-order (second- or third-order) upwind or central difference scheme plus adaptive dissipation terms are adopted to approximate the convection term; while second-order central difference schemes are used for viscous and source terms. The adaptive dissipation terms are controlled by the flowfield, and can be switched to either second order or fourth order. In this approach, a fourth-order damping is activated in smooth flow region, while a second-order damping is used near flow discontinuities such as flows through a shock regime. Hence, the stability of this damping scheme improves the numerical convergence. The formulation of the high-order upwind/central difference scheme plus adaptive dissipation methodology is detailed in Ref. 11. A predictor plus multi-corrector pressure-based solution method is employed in FDNS so that a wide range of flow speeds can be analyzed. A vectorized point iteration matrix solver is currently employed to insure a stable and fast convergence rate. A multi-block, multi-zone capability is included in the FDNS code such that problems with complex geometries can be analyzed efficiently.

PROPOSED POROSITY MODEL

The conventional porosity models assume the use of orthogonal coordinates and geometrically similar control volumes[1-2]. In the present approach, the general boundary fitted coordinate systems were incorporated in the formulation. Two new parameters, volume porosity (γ_v, defined as the ratio of the volume occupied by the fluid to the total volume) and surface porosity (γ_i, defined as the ratio of the surface area in the i-direction available for flow to the corresponding total surface area in the same direction), were introduced into the flow governing equations. For the present porosity model, equation (1) was rewritten as

$$\frac{\gamma_v}{J}\frac{\partial \rho q}{\partial t} = -\frac{\partial \gamma_i F_i}{\partial \xi_i} + \gamma_v S_q = R_q = \text{Residual} \qquad (6)$$

A distributed drag force D and a heat flux H_f source term were also added to the source terms (as shown in Eq. 4) of the momentum equation and the energy equation, respectively, to simulate the effects of resistance and heat transfer due to the presence of the LOX posts in the flow field. In the present study, only the drag force was considered in the numerical simulation. The drag force was modeled based on geometric parameters and averaged velocity around a local LOX post. Since the drag force D is defined as

$$D = 0.5 \rho u^2 C_D \qquad (7)$$

where ρ, u, and C_D are local flow density, local total velocity, and local drag coefficient, respectively, we can compute the distributed drag force by evaluating these three parameters.

2-D tube bank flow studies were conducted to verify the drag coefficients for the flow around the LOX posts assembly. Moreover, the 13th (outermost) row posts are shielded in pairs, where holes were drilled on the shield to allow flow to go through. Additional CFD validation studies were needed to identify the drag coefficients for the flow around shielded elements.

2-D TUBE BANK FLOW STUDIES

The CFD investigation of the flow through the tube bank configuration was conducted for various Reynolds numbers (Re), such as 20, 10^5, 10^6, and 10^7. Based on the CFD studies and a literature review[12-17], a drag coefficient model for the tube bank flows is proposed as shown in Table 1. The proposed model was compared with the numerical results from previous benchmark cases and relatively good agreement has been achieved.

TURBULENT FLOW AROUND SHIELDED POST ELEMENTS

In the hot gas injector region, the outer row (#13) is protected by shields to avoid damages caused by direct impingement on the LOX posts from the high speed gases. There are four types of shield, #039, #037, #025, and #023, where the configurations of shield-039 and shield-023 are sketched as shown in Figure 2. All the shields enclose two posts in one shield, except shield-025 which encloses three posts in one shield. The hole distribution on shield-025 is similar to that on shield-023, and there is only one shield-025 on row #13; hence shield-025 was modeled the same as shield-023 in the numerical analysis. Shield-037 has the same type of hole distribution as shield-039, but shield-037 does not have the wing at the end of the shield. There are six #037 shields and five #039 shields, and they are installed in an alternating sequence and are located near the fuel side. In the present porosity model, the drag coefficient for both shield-039 and shield-037 was assumed to be identical and was obtained from the numerical analysis of shield-037 geometry. Therefore, in this study all shields were considered to be of either the 023 or 037 type. CFD analyses were conducted for these two types of shields to obtain the porosity model for the flow through a shielded element.

Since the presence of the shield will greatly increase the drag force, numerical studies were performed to investigate the drag coefficient for the flow through the shielded elements with and without holes. Both 3-D and 2-D analyses were performed. Since the shielded elements are located on the outer row of the post assembly, the Reynolds number of the inlet flow to the shielded elements is relatively high and is around 10^6. An approximation for different types of holes on the shields was made to relax the requirement of using numerous grids to resolve these holes. The approximation was to treat the cross-section of various holes as rectangles with their width equal to the gap between each pair of posts. Therefore, the same drag coefficient model would be employed for various types of shields. The way to distinguish the difference between various types of shield is to identify the vertical locations of each hole and to use different porosity for different types of shields.

The numerical studies indicate that the drag coefficient does not change appreciably for the same shield geometry as the Reynolds number varies around 10^6. However, the computed

drag coefficient is about 4 for the region with holes on the shield, and is close to 48 for the region without holes.

LOSS COEFFICIENT MODEL

In addition to the drag coefficient model for the flow through tube bank environment, a loss coefficient model is required to compute the mass flow rate for the flow through various porous media, such as an individual LOX post, porous plates, and boundary layer control (BLC) holes. To relate the mass flow rate and pressure drop across the porous media, the following loss coefficients (K) are defined.

$$K = \frac{\rho \, \Delta p}{\dot{m}^2} \, , \qquad \Delta p = p - p_{chamber} \, , \quad \text{or} \quad \Delta p = p - p_{baffle} \qquad (8)$$

where ρ, p are the density and static pressure at the exit flow location, and $\dot{m}$ is the mass flow rate through a porous medium. $p_{chamber}$ and p_{baffle} are the static pressure in the combustion chamber near the injector plate and near the end of baffle elements, respectively. In the present study, the values of $p_{chamber}$ and p_{baffle} were held constant, where in the actual hot fire test they can vary in both radial and circumferential directions. The value of the loss coefficient (K) for each porous medium will be given later in the NUMERICAL RESULTS section. Therefore, the exit mass flow rate through each porous medium was computed based on the distributions of local loss coefficient and local exit pressure. In the numerical analysis, the area for each porous medium is different at each radial location; however, this is not true in the real geometry. Hence, in the computational domain, the area effect was excluded from the mass flow rate calculation. The assembly of the loss coefficients in the computational domain is then defined as

$$K' = \frac{\rho \, \Delta p}{\dot{M}^2} \, , \quad \text{i.e.} \quad \dot{M} = \sqrt{\frac{\rho \, \Delta p}{K'}} \qquad (9)$$

where K' and $\dot{M}$ are the global loss coefficient and exit mass flow rate for a type of porous medium, respectively. Hence, the local mass flow rate $\dot{m}$ can be calculated as

$$\dot{m} = \dot{M} \frac{A_i}{A} = \frac{A_i}{A} \sqrt{\frac{\rho \, \Delta p}{K'}} \qquad (10)$$

where A and A_i denote the global and local exit areas for the same type of porous medium, respectively. The value of the global loss coefficient (K') for each porous medium will also be reported later in next section.

NUMERICAL RESULTS

8

The 3-D porosity/CFD analysis of the SSME main injector assembly was performed for the phase II+ power head geometry at the 104% power balance level. The entire configuration was divided into three components: 1) LOX dome, 2) hot gas injector assembly, and 3) hydrogen cavity. The overall mass flow rate distribution and mixture ratio distribution was calculated by superimposing the results from these three components. The numerical computation for these three components was conducted independently, except the calculated exit pressure of the hot gas injector assembly was employed as the back pressure for the secondary face plate in the hydrogen cavity region. At the 104% power balance level, the exit pressure to the combustion chamber $P_{chamber}$ was estimated to be about 3135 psi, where the exit pressure from baffle elements P_{baffle} was roughly equal to 3084 psi.

LOX DOME

The LOX dome geometry was simulated as shown in Figure 3 with a 62 x 91 x 16 mesh system. The bleed pipes to the first three rows of the LOX posts were omitted and were replaced with the exit flow through the nose region. This simplification greatly reduced the number of grid points required to describe the details of the bleed pipe geometry. The importance of the mass flow rate distribution for the first three rows of the LOX post was mitigated by the 1-D analytical result which indicates that the magnitude of the mass flow rate is relatively uniform among these three rows. The numerical analysis was conducted based on incompressible, adiabatic, turbulent flow with single species (liquid oxygen). The inlet flow conditions and loss coefficients are listed in Table 2 and 3, respectively. Uniform inlet velocity profiles were used because no other information was available at the LOX tee exit.

Based on the above inlet flow conditions and the proposed loss coefficient model, a 3-D numerical computation was performed. Figure 4, top view of the velocity vector plot, exhibits the LOX flow around the LOX dome. The cross-sectional views of the two velocity vector planes in Figure 4, -90° (fuel side) and 90° (oxidizer side) planes, are plotted as shown in Figures 5a-5b. It is clearly shown that two recirculation zones occur in the plane with inlet flow, but a very smooth flow structure is formed in the plane without inlet flow. It can be seen that the exit flow velocities are fairly uniform in each cross section. This is consistent with the static pressure distribution at the exit plane. The static pressure contours at the LOX dome exit plane are drawn in Figure 6. Although it seems higher pressure around the planes with inlet flow, the overall pressure difference is very small, which indicates a fairly uniform exit pressure.

HOT GAS INJECTOR ASSEMBLY

The computational domain for the hot gas injector assembly consists of three zones: 1) LOX post assembly torus, 2) fuel transfer duct, and 3) oxidizer transfer duct. A 37 x 91 x 25 mesh system was employed for the LOX post assembly torus, and a 10 x 21 x 17 mesh system was used for the fuel transfer duct, while the oxidizer transfer duct was described by a 10 x 15 x 15 grid system. The geometry and the grid system of the hot gas injector assembly is plotted as shown in Figure 7. The hot gases coming out of the fuel preburner and the oxidizer preburner enter the main injector assembly through the fuel transfer duct and the oxidizer transfer duct,

9

respectively. The inlet flow conditions to both transfer ducts are tabulated in Table 4. The inlet velocity and pressure profiles of the hot gas flow to the fuel transfer duct were interpolated based on the numerical results by Yang, and his coworkers[18], while the inlet profiles to the oxidizer transfer duct were interpolated based on the image of Yang's results.

The loss coefficient distribution used in the LOX post assembly was based on the air flow test data for various post elements. The value of the loss coefficients is listed in Table 5. K is the measured loss coefficient for each single post, while K' is the loss coefficient for each type of the posts in the computational domain. According to Equations (8-9), the relation between K and K' is

$$K' = \frac{\rho \, \Delta p}{\dot{M}^2} = \frac{\rho \, \Delta p}{(N\dot{m})^2} = \frac{K}{N^2} \tag{11}$$

where N is the number of each type of post elements. Since there is no hot gas flow through baffle elements, the loss coefficient for these elements was set to infinity.

The numerical analysis for the hot gas injector assembly was conducted based on symmetrical, incompressible, isothermal, turbulent, no-reacting flow with two species (hydrogen and oxygen). Special attention was paid to the distribution of the porosity and of the drag coefficient on the 13th-row elements to identify the presence of holes on the shield. The predicted velocity vectors at the symmetrical plane are drawn as shown in Figure 8. It appears that the hot gas is deflected by the shielded elements (the outermost row), and passes through the non-shielded area of the posts. In addition, the exit velocity of the hot gas seems to be very uniform, except at the baffle elements through which there is no hot gas exit to the injector face. The deflected hot gas not only passes through the non-shielded area of the posts, but also sweeps around the torus, which can be seen from the velocity vector plots as shown in Figures 9-10. The hot gases from the fuel and the oxidizer sides flow into the region between the LOX posts and out into the main combustion chamber. Due to more mass flow rate through the fuel transfer duct, the fuel side gases penetrate much further into a horizontal plane around the LOX-post region. Significant mixing occurs where the hot gases from the two sides of the engine meet. The exit velocity contours of the hot gas through the injector face are plotted in Figure 11. This figure shows that the exit velocity of the hot gas is somewhat larger near the fuel side than near the oxidizer side; however, the difference is very small which indicates that the flow is nearly uniform except at the baffle elements. The hot gas static pressure distribution at the exit plane of hot gas injector assembly exhibits the same characteristics as that of the exit velocity. The mixture ratio of the hot gas exit to the injector face is uniformly increased from the fuel side towards the oxidizer side as indicated in Figure 12, where the discontinuity at the symmetry plane is due to the linear extrapolation from interior points.

HYDROGEN CAVITY

The hydrogen cavity region was descritized into a 29 x 91 x 14 mesh system, and is sketched as shown in Figure 13. The inlet flow conditions are listed in Table 6 based on 104%

power balance. The inlet velocity profile was assumed to be uniform everywhere, and all velocity vectors were directed towards the center of radius.

The loss coefficient model is listed in Table 7, where the mass flow rate through each porous medium was based on 1-D analytical results. The back pressure of the secondary face plate (top surface) was set to be 3288 psi from the hot gas injector assembly numerical result. An assumption was made that all hydrogen flow exiting through the secondary face plate to the hot gas region passed through the non-baffle elements and exited at the injector face. Therefore, in the post processing, the mass flow rate through the secondary face plate was added to the mass flow rate through the primary face plate (bottom surface) at the same grid location.

The 3-D numerical analysis for the hydrogen cavity region was performed based on symmetrical, incompressible, adiabatic, turbulent flow with single species (hydrogen). The numerical result, as shown in Figure 14, indicates that a recirculation zone occurs as the fuel flow enters the hydrogen cavity through a narrow gap. It also reveals that the velocity of the flow exit through the baffle elements is quite uniform, and is much larger than that exit through porous plates. The flow exit through BLC holes has the largest velocity, but the exit mass flow rate is relatively small due to small exit area. The numerical result shows the static pressure distributes very uniformly at the primary face plate surface.

MAIN INJECTOR ASSEMBLY

After conducting the numerical computation for the three components of the main injector assembly, a post processing calculation was made in order to obtain the overall O/F ratio at the injector face. By superimposing the exit mass flow rates and the mass fractions of hydrogen and oxygen from the three components of the main injector assembly, the mixture ratio distribution at the injector face was obtained as shown in Figure 15. It appears that the highest O/F ratio occurs near the baffle elements. The O/F ratio distribution also exhibits higher mixture ratio near the fuel side than that near the oxidizer side. The O/F distribution in the circumferential direction is of great interest, especially near the outer edge of the injector face, and so it is plotted as shown in Figures 16 & 17, respectively. Figure 16 plots the value without adding BLC coolant flow in the O/F ratio calculation, while Figure 17 shows the O/F ratio with BLC coolant flow added. Each spike in the mixture ratio plots occurs at baffle elements. The O/F ratio distribution in the radial direction is displayed in Figures 18 & 19, which shows the mixture ratio at the plane of -90° (on the fuel side) and 90° (on the oxidizer side), respectively. The plots reveal that the O/F ratio is close to stoichiometric around baffle elements.

CONCLUSIONS AND RECOMMENDATIONS

The 3-D CFD/porosity analysis reveals that the mass flow rate at the injector face is relatively uniform. The predicted mixture ratio is close to stoichiometric (O/F = 8) around baffle element at 104% power balance level, which might cause very hot spots around baffle elements. However, due to the many assumptions made in the porosity model and the use of a very coarse

11

grid system, the numerical results can only provide a qualitative trend. As can be seen from the loss coefficient model, the local mass flow rate distribution is dependent on both the pressure drop and the loss coefficient distributions. Hence, the assembly of the loss coefficient model is critical to the numerical result, and the availability of the measured loss coefficients for each porous medium will greatly improve the CFD analysis. In addition, the distribution of chamber pressure and of baffle element discharge pressure was assumed to be uniform in this study; hence, the CFD/porosity model can be improved if the actual distribution of discharge pressure were known and specified in the calculation. Meanwhile, a proper inlet flow profile to the LOX dome and to the hydrogen cavity can help the developed model to predict the flow field more accurately. The developed CFD/porosity model should be further tested at different power balance levels. The numerical results of this study should be used as the inlet conditions to the combustion chamber in order to predict the engine performance and heat loads of the chamber.

REFERENCES

[1] Sha, W.T., "Summary of Methods Used in Rod-Bundle Thermal-Hydraulic Analysis," in Turbulent Force Convection in Channels and Bundles, Vol. 1, Ed. S. Kakac and D.B. Spalding, McGraw-Hill International Book Company, pp. 279-299, 1979.

[2] Soo, S.L., and Sa, W.T., "Porous Medium Formulation of Three-Dimensional Transient Flow Through Rod Bundles," in Turbulent Force Convection in Channels and Bundles, Vol. 1, Ed. S. Kakac and D.B. Spalding, McGraw-Hill International Book Company, pp. 301-323, 1979.

[3] Sha, W.T., and Thompson, J.F., "Rod-Bundle Thermal Hydraulic Analysis Using Boundary Fitted Coordinate System," NUREG-CR-0001, ANL-78-1, Jan. 1978.

[4] Coucaud, O., Morel, P., and Caltagirone, J.P., "Numerical Modeling on Non-Linear Effects in Laminar Flow Through a Porous Medium," Journal of Fluid Mechanics, Vol. 190, 1988, pp. 393-407.

[5] Chen, Y.S., "Compressible and Incompressible Flow Computations with a Pressure Based Method," AIAA Paper 89-0286, AIAA 27th Aerospace Sciences Meeting, Reno, Nevada, Jan. 1989.

[6] Wang, T.S., Chen, Y.S., and Farmer, R.C., "Numerical Study of Reactive Ramjet Dump Combustor Flowfields with a Pressure Base CFD Method," AIAA Paper 89-2798, AIAA 25th Joint Propulsion Conference, Monterey, CA, July 10-12, 1989.

[7] Chen, Y.S., Cheng, G.C., and Farmer, R.C., "Reacting and Non-Reacting Flow Simulation for Film Cooling in 2-D Supersonic Flows," AIAA Paper 92-3602, AIAA 28th Joint Propulsion Conference and Exhibits, Nashville, TN, July 6-8, 1992.

[8] Chen, Y.S., and Kim, S.W., "Computation of Turbulent Flows Using an Extended k-ε Turbulence Model," NASA CR-179204, Oct. 1987.

[9] Monson, D.J., Seegmiller, H.L., McConnaughey, P.K., and Chen, Y.S., "Comparison of Experiment with Calculations Using Curvature-Corrected Zero and Two Equation Turbulence Models for a Two-Dimensional U-Duct," AIAA Paper 90-1484, AIAA 21st Fluid Dynamics, Plasma Dynamics and Lasers Conference, June 18-20, 1990.

[10] Liakopoulos, A., "Explicit Representations of the Complete Velocity Profile in a Turbulent Boundary Layer," AIAA Journal, Vol. 22, June, 1984, pp. 844-846.

[11] Cheng, G.C., Chen, Y.S., Garcia, R., and Williams, R.W., "Numerical Study of 3-D Inducer and Impeller for Pump Model Development," AIAA Paper 93-3003, AIAA 24th Fluid Dynamics Conference, Orlando, FL, July 6-9, 1993.

[12] White, F.M., Heat and Mass Transfer, Addison-Wesley Publishing Co., Inc., 1988.

[13] Stasiulevičius, J., and Skrinska, A., Heat Transfer of Finned Tube Bundles in Crossflow, Hemisphere Publishing Co., New York, 1988.

[14] Žukauskas, A., and Ulinskas, R., Heat Transfer in Tube Banks in Crossflow, Hemisphere Publishing Co., New York, 1988.

[15] Žukauskas, A.A., and Kalinlin, E.K., "Enhancement of Heat Transfer," in Heat Transfer Soviet Reviews, Vol 2, Hemisphere Publishing Co., New York, 1989.

[16] Žukauskas, A., "Heat Transfer from Tubes in Crossflow," Advances Heat Transfer, Vol. 8, pp. 93-160, 1972

[17] Žukauskas, A., and Ulinskas, R., "Banks of Plain and Finned Tubes," in Heat Exchanger Design Handbook, Vol. 2, Hemisphere Publishing Co., New York, 1984.

[18] Yang, R.J., Lin, S.J., and Chang, J.L.C., "Numerical Simulation of Flowpaths in the SSME Hot Gas Manifold," 5th SSME Computational Fluid Dynamics Workshop Meeting, Huntsville, Alabama, April, 1987.

Table 1. The Drag Coefficient Model for Tube Bank Flow

	C_D
$Re < 4 \times 10^3$	$0.417 \, EXP(4.932 \, Re^{-0.296})$
$4 \times 10^3 < Re < 6 \times 10^4$	$0.647 - 0.5 \times 10^{-6} Re$
$6 \times 10^4 < Re < 10^6$	$0.618 + 0.491 \times 10^{-6} Re - 6.303 \times 10^{-12} Re^2 + 10.694 \times 10^{-18} Re^3 - 5.2 \times 10^{-24} Re^4$
$Re > 10^6$	0.2735

Table 2 Inlet Flow Conditions to the LOX Dome (104% RPL)

Static Pressure	Static Temperature	Reynolds Number	Mass Flow Rate
3670 psi	197 °R	$1.28 \times 10^8 \, ft^{-1}$	826.7 lb/sec

Table 3 The Loss coefficient model for the LOX dome region (104% RPL)

	$\dot{m}$ (lb/sec)	K (ft^{-4})	$\dot{M}$ (lb/sec)	K' (ft^{-4})
Non-Baffle Elements	1.38	9.62×10^7	665.105	4.14×10^2
Baffle Elements	1.433	9.78×10^7	105.65	1.79×10^4
First Three Rows	1.332	1.03×10^8	56.154	5.81×10^4

Table 4 The Inlet Flow Conditions to the hot gas injector Assembly (104% RPL)

	Pressure (psi)	Temperature (°R)	Reynolds no. (ft^{-1})	Mass Flow Rate (lb/sec)	O/F Ratio
Fuel Side	3351	1666	3.17×10^7	77.55 (in half)	0.8685
LOX Side	3353	1254	7.88×10^7	33.38 (in half)	0.599

Table 5 The Loss Coefficients for the Hot Gas Flow Through the LOX Post

	Non-Baffle Elements			Baffle-Elements
	Row #13	Row #12	Row #1 - #11	
K (in^{-4})	135	156	152	∞
K' (ft^{-4})	4.374 x 10^2	5.751 x 10^2	23	∞

Table 6 Inlet Conditions of the Fuel into Hydrogen Cavity Region (104% RPL)

Pressure (psi)	Temperature (°R)	Reynolds no. (ft^{-1})	Mass Flow Rate (lb/sec)
3395	449	2.52 x 10^7	14.55 (in half)

Table 7 The Loss Coefficient Model Used in the Hydrogen Cavity Region (104% RPL)

	$\dot{m}$ (lb/sec)	Δp (psi)	K' (ft^{-4})
Primary Face Plate	6.77	251	3.578 x 10^4
Secondary Face Plate	3.41	98	5.506 x 10^4
Baffle Elements	15.25	301	8.467 x 10^3
Non-Baffle Elements	0	251	∞
BLC Holes	3.67	251	1.16 x 10^5

Figure 1

Computational Domain

Shield-037   Shield-025
Shield-039   Shield-023

SHIELD   T-BOLT   T-BOLT   SHIELD
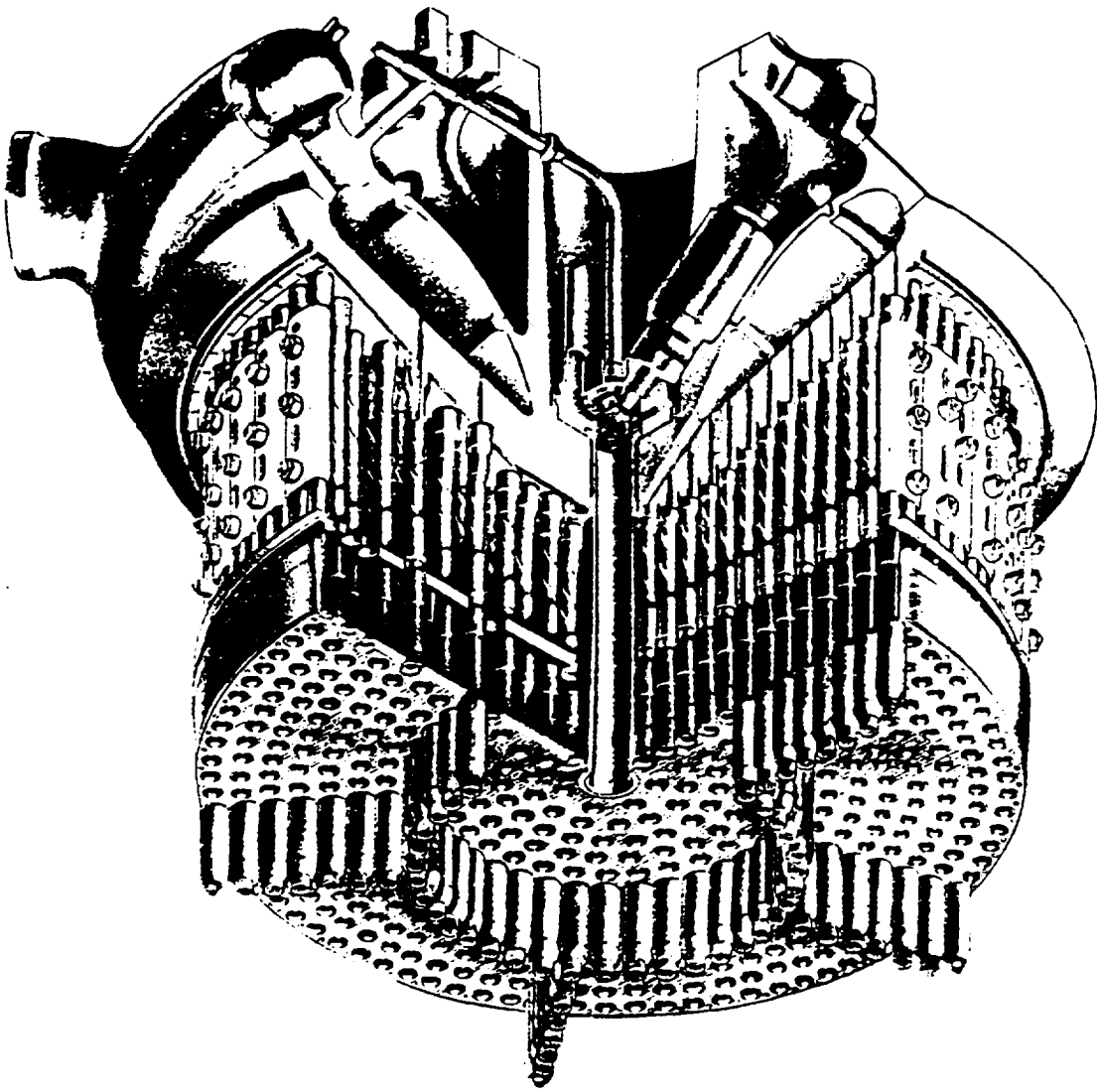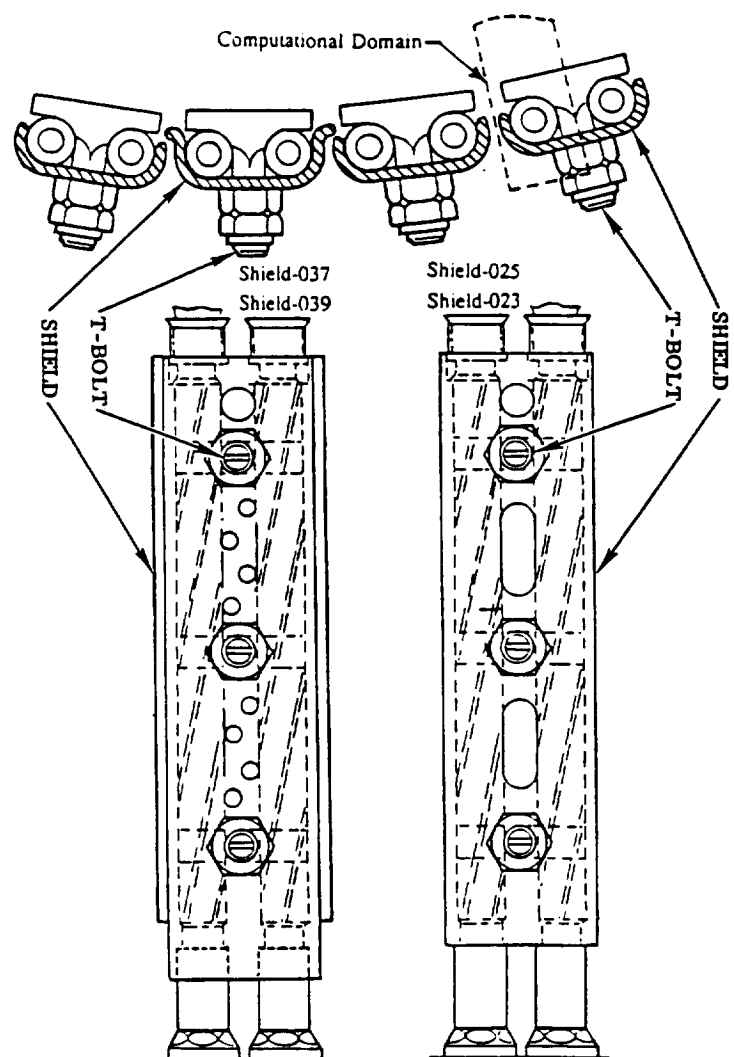
Figure 2

Figure 3

Figure 4

(a) −90°

(b) 90°
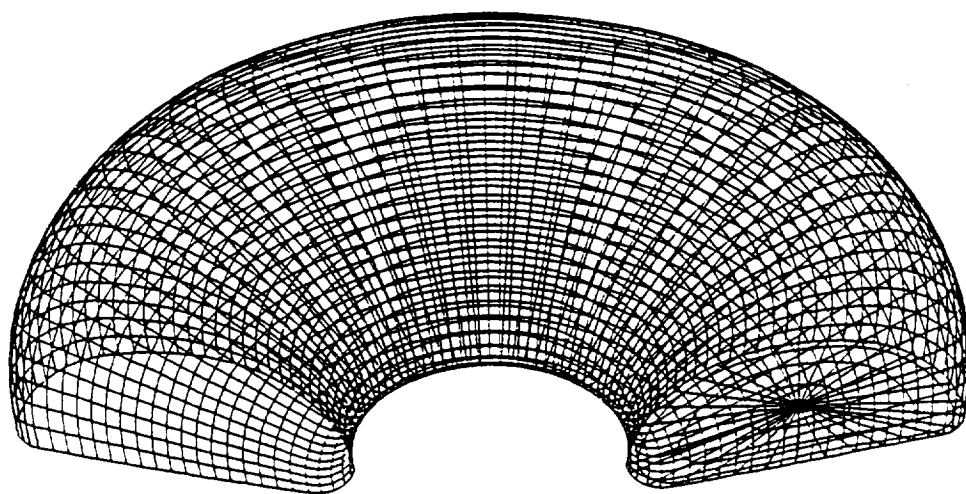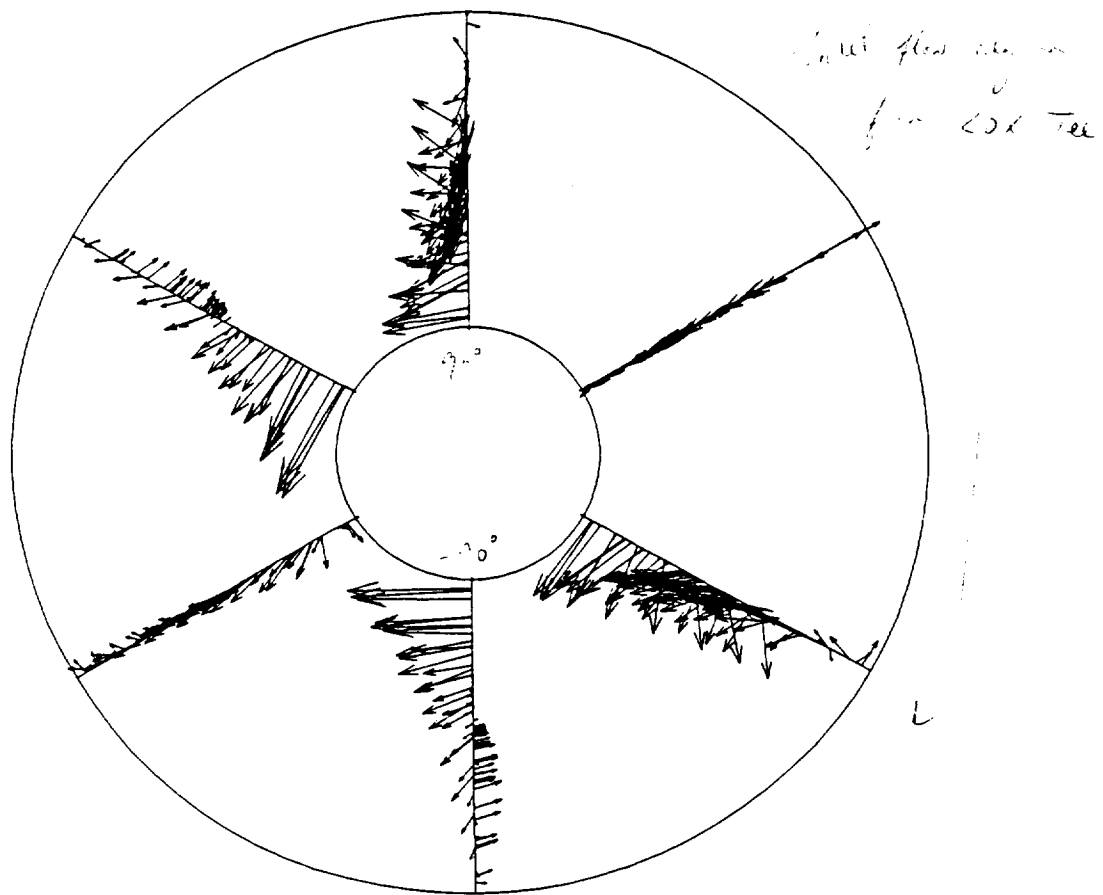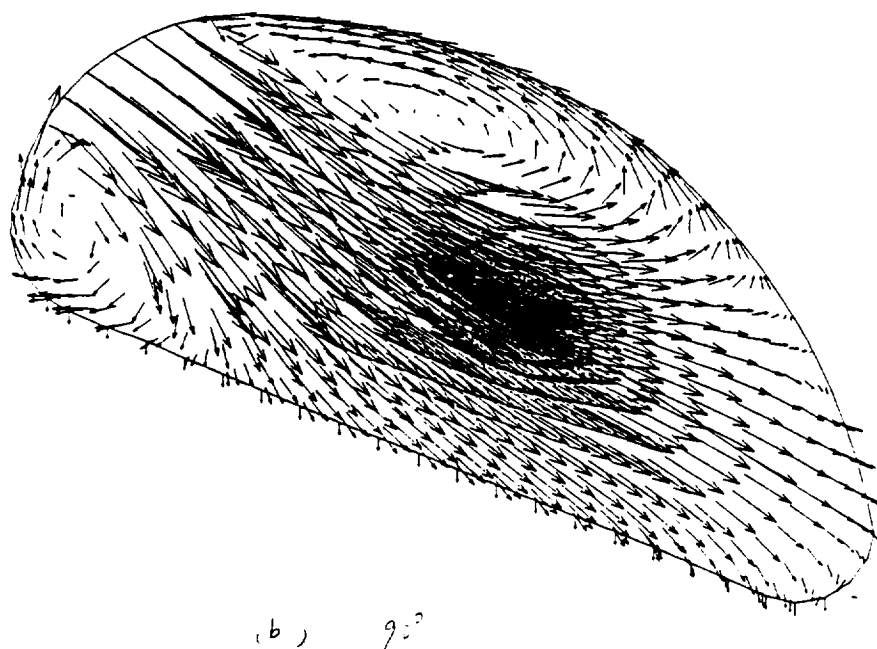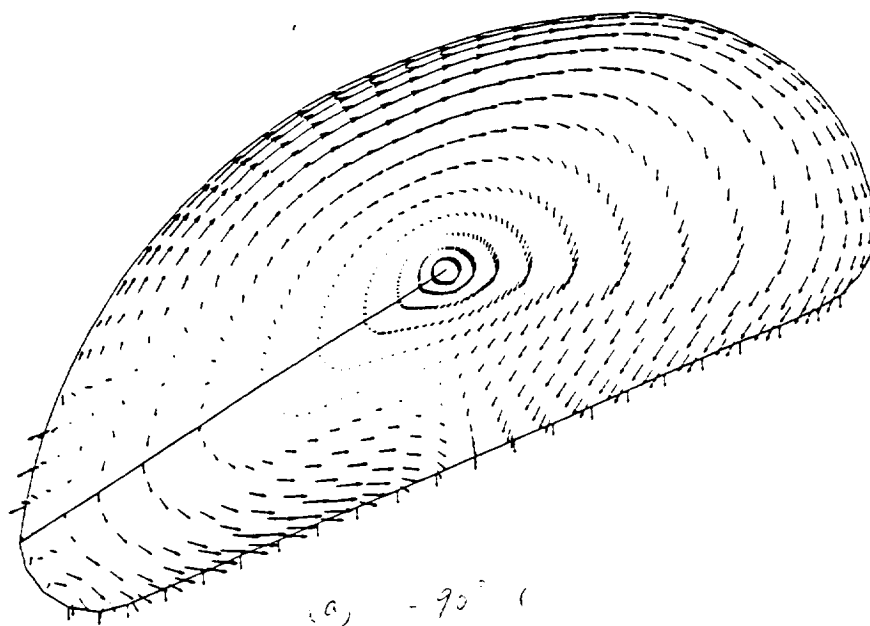
Figure 5
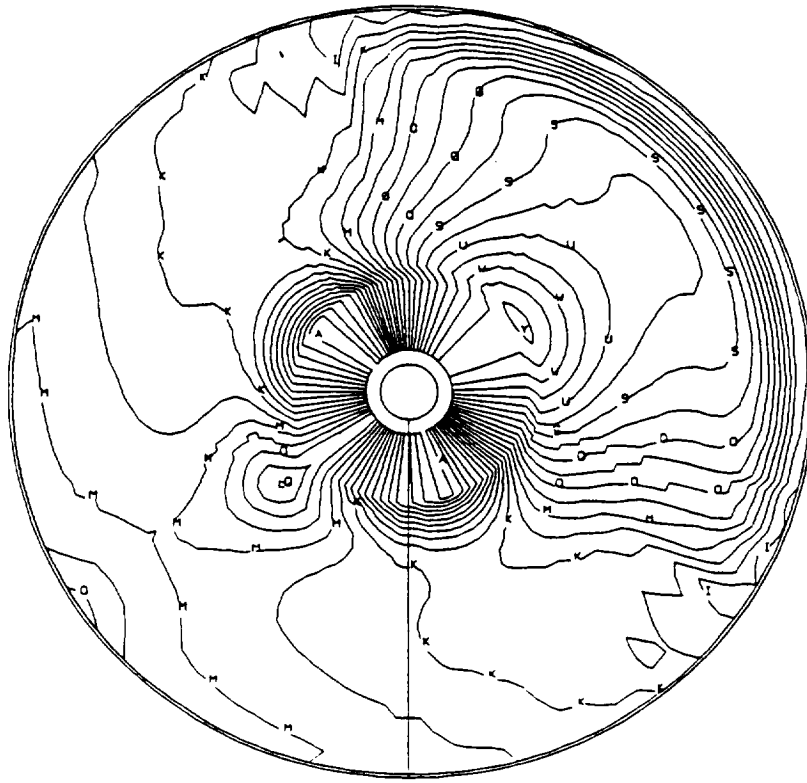
ID	VALUES
A	5 2749E+05
B	5 2799E+05
C	5 2849E+05
D	5 2899E+05
E	5 2949E+05
F	5 2999E+05
G	5 3049E+05
H	5 3099E+05
I	5 3149E+05
J	5 3199E+05
K	5 3249E+05
L	5 3299E+05
M	5 3349E+05
N	5 3399E+05
O	5 3449E+05
P	5 3499E+05
Q	5 3549E+05
R	5 3599E+05
S	5 3649E+05
T	5 3699E+05
U	5 3749E+05
V	5 3799E+05
W	5 3849E+05
X	5 3899E+05
Y	5 3949E+05

Figure 6
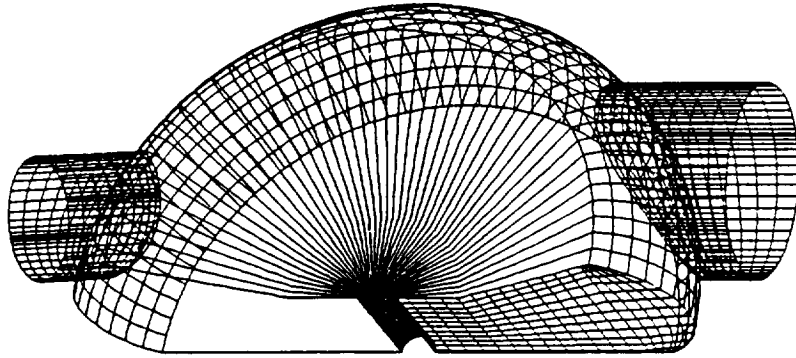
Figure 7

XMIN -9 9746E-01
XMAX 9 9746E-01
YMIN -1 1162E+00
YMAX 5 4617E-01
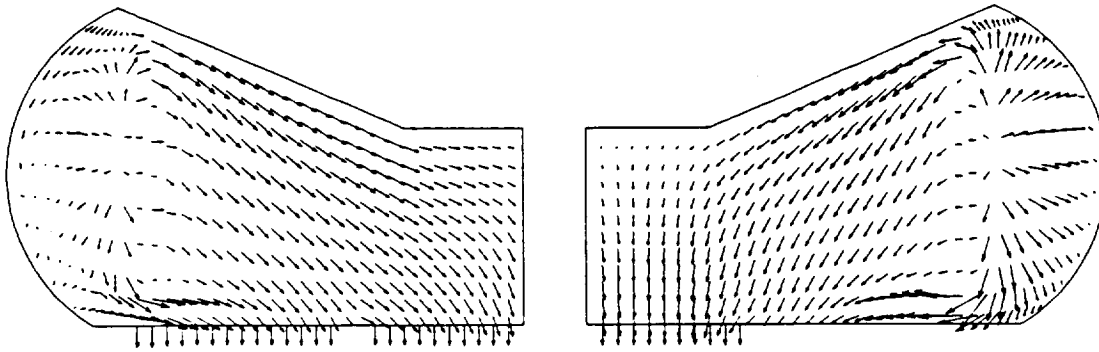
Figure 8
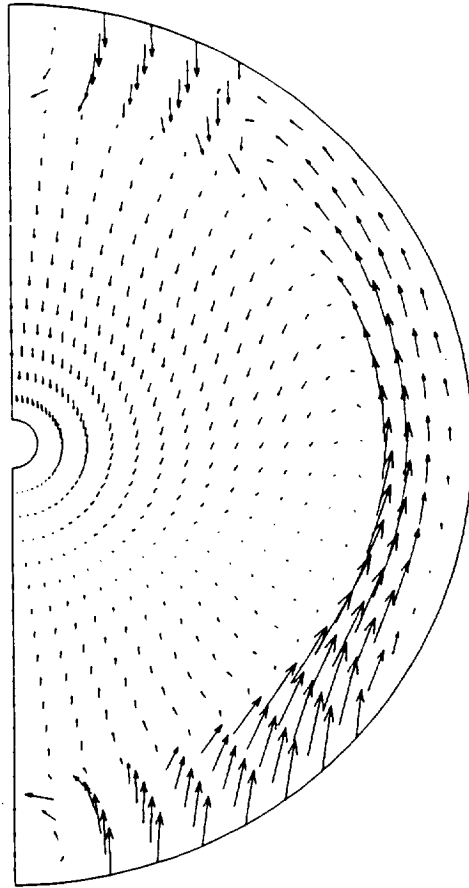
XMIN -7 2197E-01
XMAX   1 6719E+00
YMIN -9 9746E-01
YMAX   9 9746E-01

Figure 7
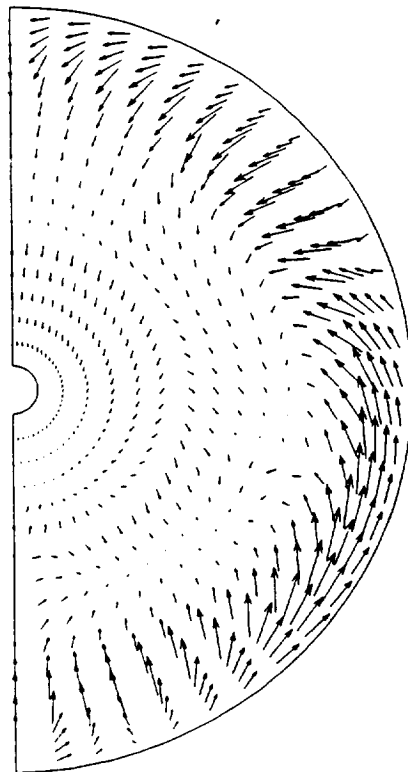
XMIN -7 2197E-01

XMAX 1 6719E+00

YMIN -9 9746E-01

YMAX 9 9746E-01

Figure 15

LOX POST ASSEMBLY TORUS, EXIT FLOW VELOCITY CONTOURS (FT/S)
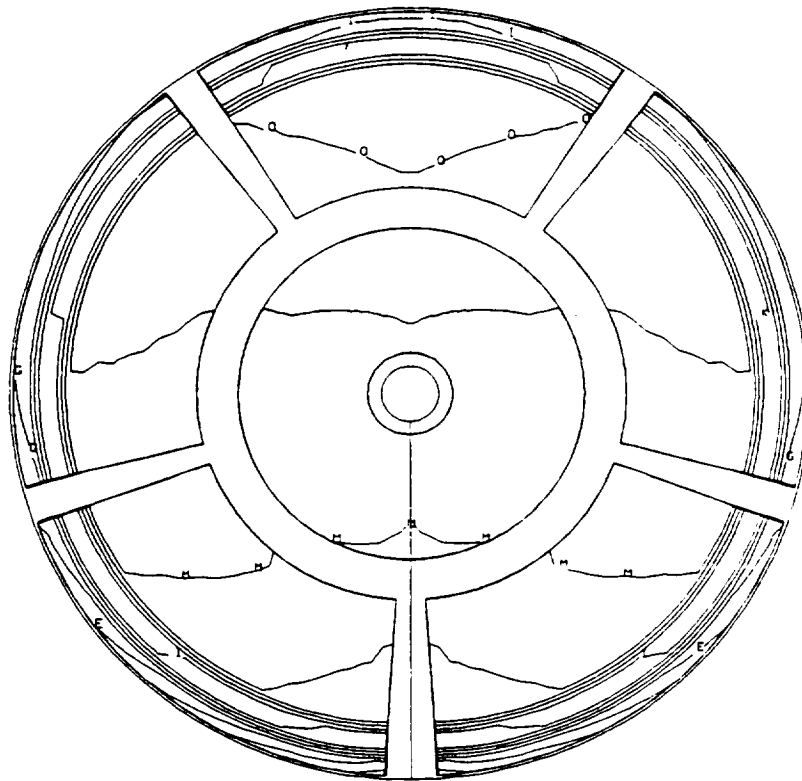
XMIN -9.2189E-01
XMAX 9.2189E-01
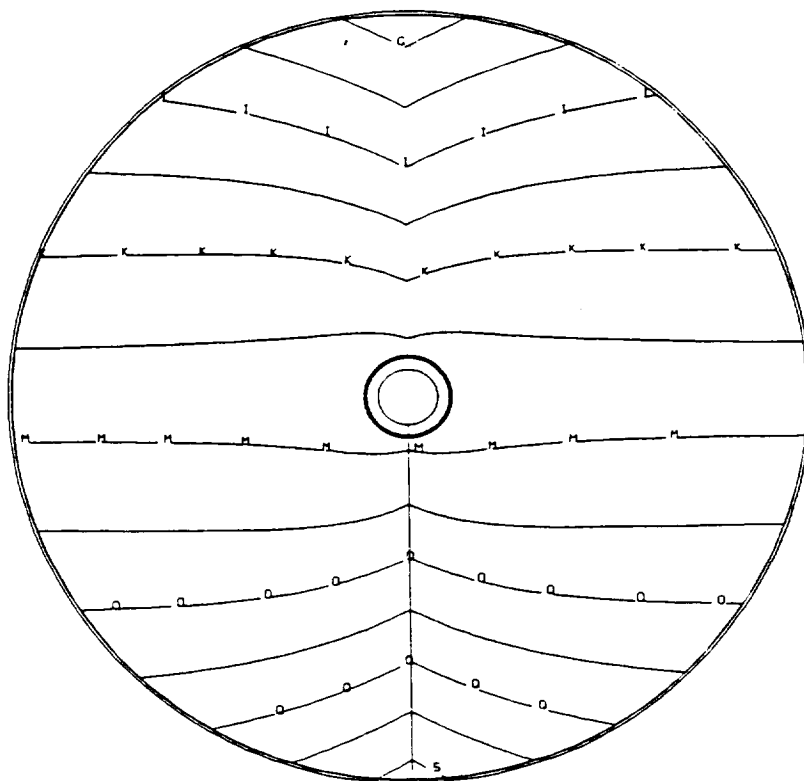YMIN -7.6824E-01
YMAX 7.6824E-01

FMIN -6.3470E+01
FMAX 0.0000E+00
DELF 9.9998E-01

CONTOUR LEVELS

ID   VALUES
A -6.3999E+01
B -6.2999E+01
C -6.1999E+01
D -6.0999E+01
E -5.9999E+01
F -5.8999E+01
G -5.7999E+01
H -5.6999E+01
I -5.5999E+01
J -5.4999E+01
K -5.3999E+01
L -5.2999E+01
M -5.1999E+01
N -5.0999E+01
O -4.9999E+01
P -4.8999E+01

LOX POST ASSEMBLY TORUS. EXIT O/F RATIO CONTOURS

XMIN -9 2189E-01
XMAX 9 2189E-01
YMIN -7 6824E-01
YMAX 7 6824E-01

FMIN 0 0000E+00
FMAX 8 2571E-01
DELF 1 4999E-02

CONTOUR LEVELS

ID	VALUES
A	5 4999E-01
B	5 6499E-01
C	5 7999E-01
D	5 9499E-01
E	6 0999E-01
F	6 2499E-01
G	6 3999E-01
H	6 5499E-01
I	6 6999E-01
J	6 8499E-01
K	6 9999E-01
L	7 1499E-01
M	7 2999E-01
N	7 4499E-01
O	7 5999E-01
P	7 7499E-01
Q	7 8999E-01
R	8 0499E-01
S	8 1999E-01
T	8 3499E-01
U	8 4999E-01

Figure 12

GRID SYSTEM OF THE HYDROGEN CAVITY (29 X 91 X 14)

XMIN -6 6273E-01
XMAX   7 8543E-01
YMIN -5 4447E-01
YMAX   6 6232E-01

Figure 13

HYDROGEN CAVITY, VELOCITY VECTORS AT SYMMETRY PLANE

XMIN -7 7284E-01
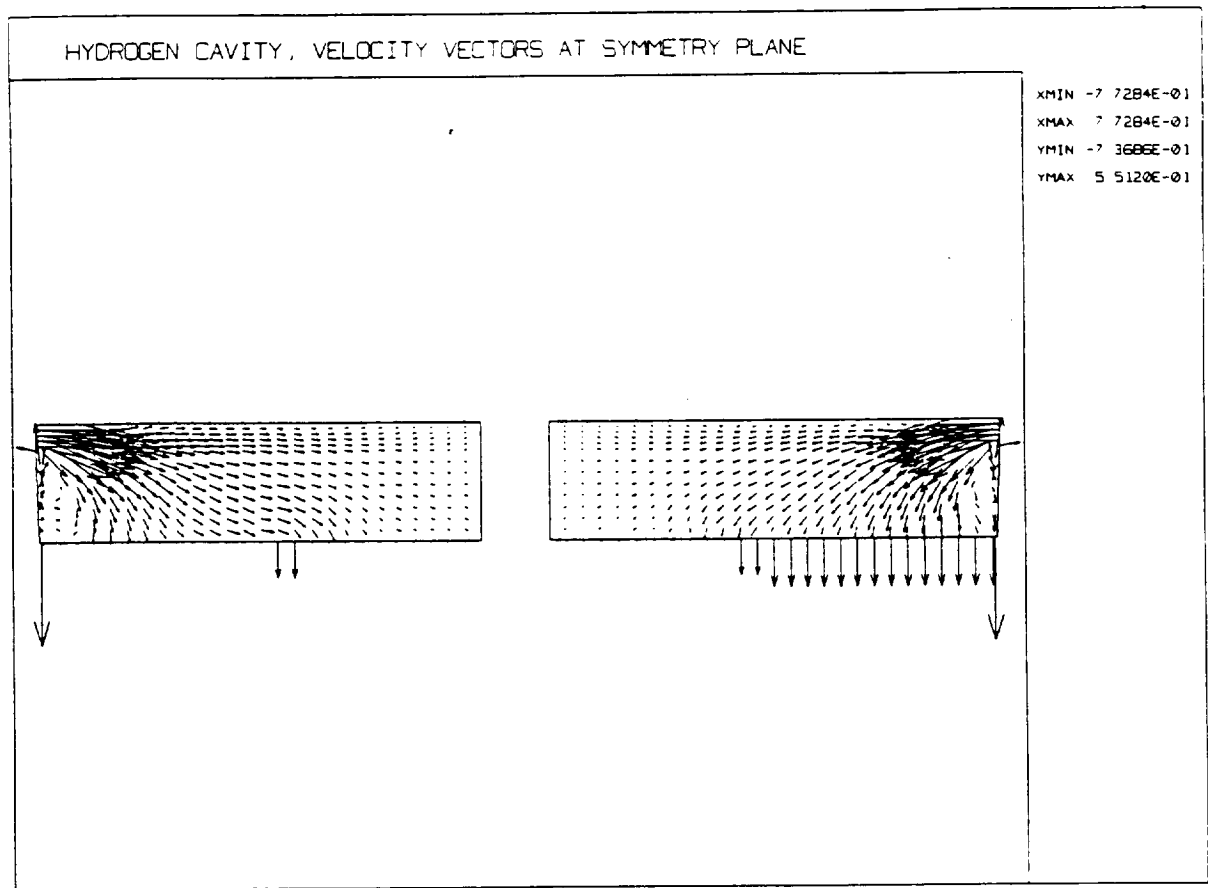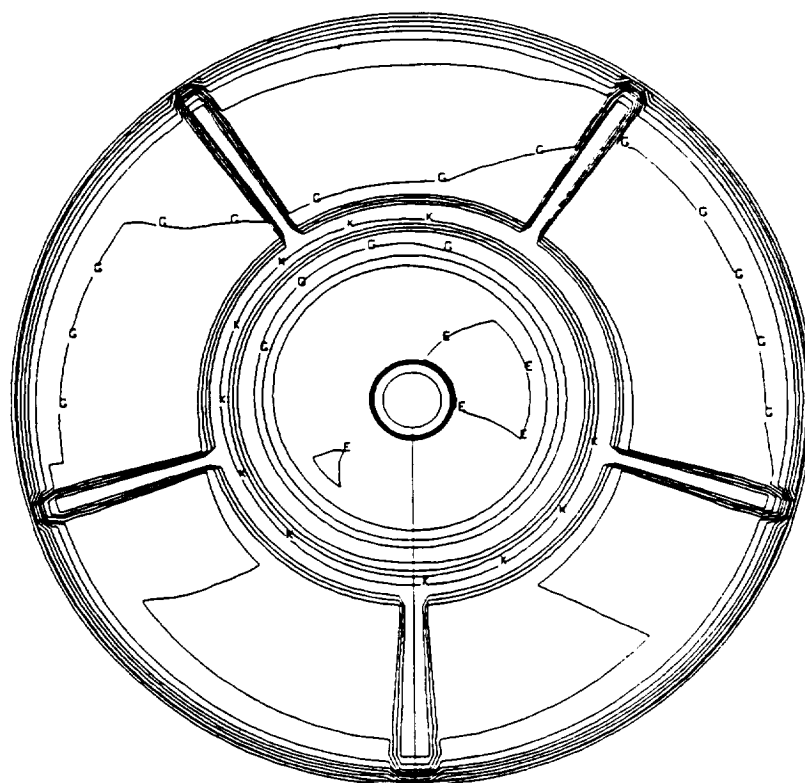XMAX 7 7284E-01
YMIN -7 3686E-01
YMAX 5 5120E-01
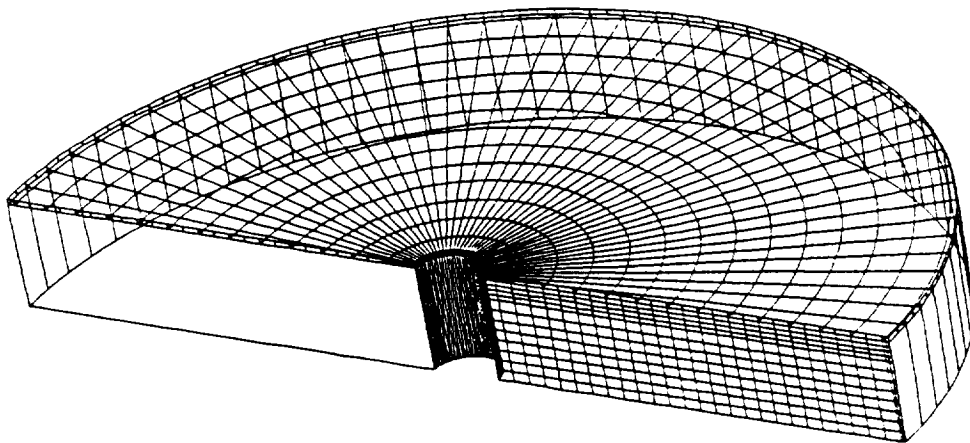
Figure 16

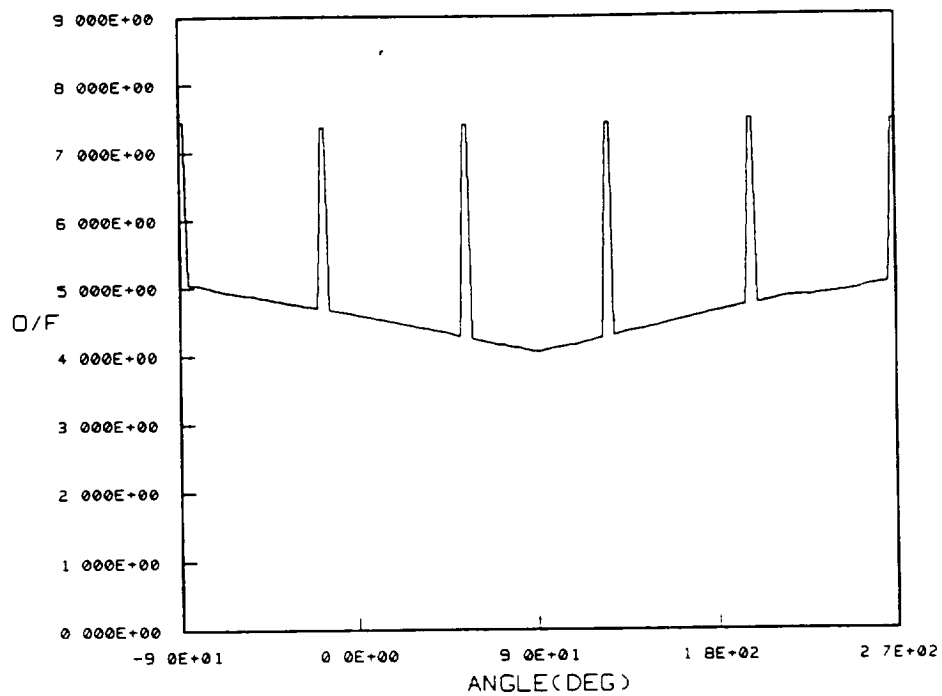O/F RATIO CONTOURS OF THE SSME MAIN INJECTOR ASSEMBLY (104%)

XMIN -9 2189E-01
XMAX 9 2189E-01
YMIN -7 6824E-01
YMAX 7 6824E-01

FMIN 0 0000E+00
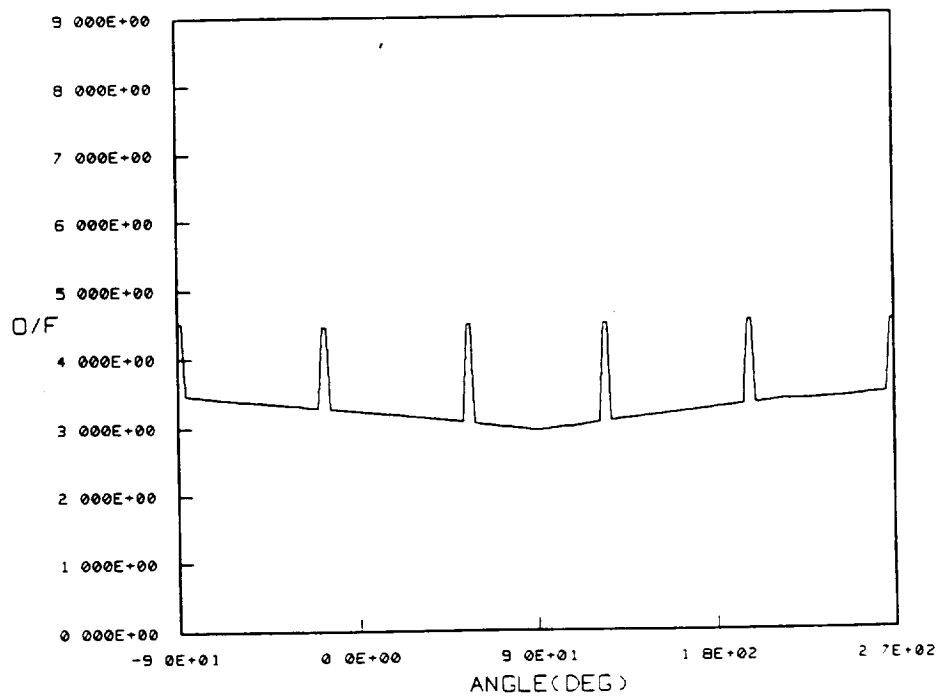FMAX 8 4866E+00
DELF 4 9999E-01

CONTOUR LEVELS

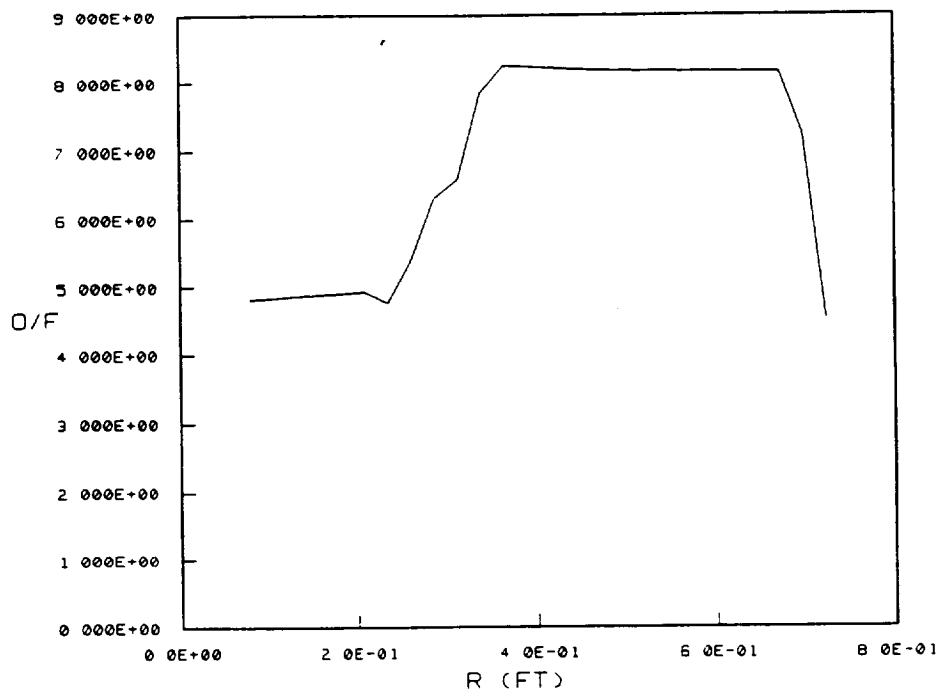| ID	VALUES
A	2 9999E+00
B	3 4999E+00
C	3 9999E+00
D	4 4999E+00
E	4 9999E+00
F	5 4999E+00
G	5 9999E+00
H	6 4999E+00
I	6 9999E+00
J	7 4999E+00
K	7 9999E+00
L	8 4998E+00

Figure 15

THE O/F RATIO DISTRIBUTION ALONG THE OUTER EDGE
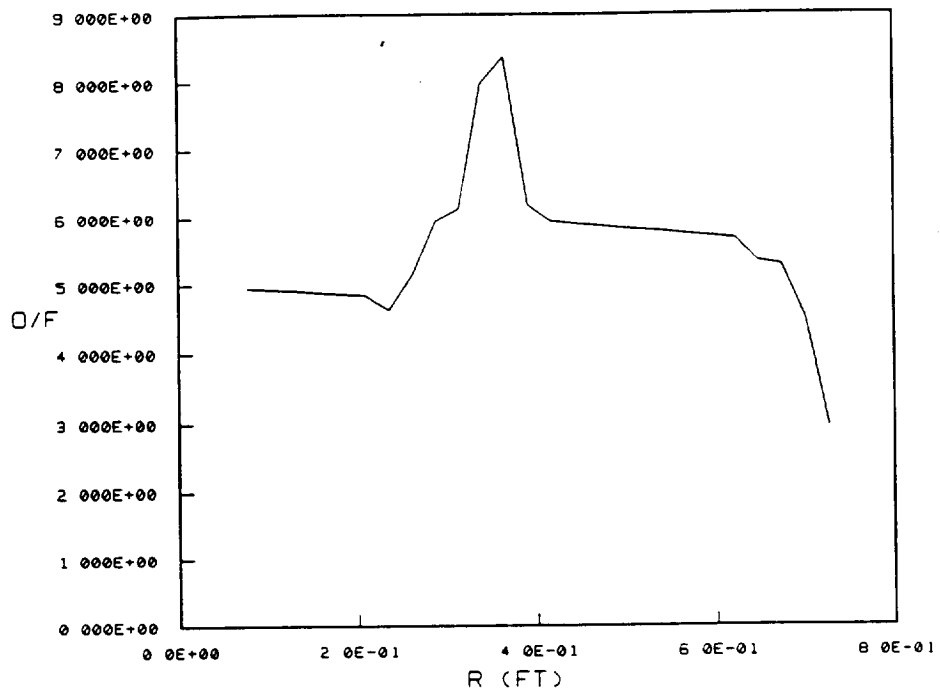OF THE INJECTOR FACE (NO BLC COOLANT ADDED)

Figure 6

THE O/F RATIO DISTRIBUTION ALONG THE OUTER EDGE
OF THE INJECTOR FACE (WITH BLC COOLANT ADDED)

Figure 17

THE O/F RATIO DISTRIBUTION AT -90 DEG (FUEL SIDE) OF THE
INJECTOR FACE (WITH BLC COOLANT ADDED)

Figure 18

THE O/F RATIO DISTRIBUTION AT 90 DEG (OXIDIZER SIDE) OF THE INJECTOR FACE (WITH BLC COOLANT ADDED)

Figure 19